Electron beam pumping improves the conversion efficiency of low-frequency photons radiated by perovskite quantum dots

Peng Du(杜鹏)[1], Yining Mu(母一宁)[1,†], Hang Ren(任航)[1], Idelfonso Tafur Monroy[2,‡], Yan-Zheng Li(李彦正)[1], Hai-Bo Fan(樊海波)[3,4,§], Shuai Wang(王帅)[1], Makram Ibrahim[5,¶], and Dong Liang(梁栋)[1]

[1] *School of Physics, Changchun University of Science and Technology, Changchun* 130022, *China*
[2] *Institute for Photonic Integration, Eindhoven University of Technology, Eindhoven* 5600 *MB, Netherlands*
[3] *Science and Technology on Low-Light-Level Night Vision Laboratory, Xi'an* 710018, *China*
[4] *Kunming Institute of Physics, Kunming* 650221, *China*
[5] *Solar and Space Research Department, National Research Institute of Astronomy and Geophysics (NRIAG), Cairo* 11421, *Egypt*

(Received 22 March 2022; revised manuscript received 19 July 2022; accepted manuscript online 22 July 2022)

This research argues that using an electron beam with high kinetic energy to pump perovskite quantum dots can significantly boost the efficiency of the low-frequency photon radiation conversion. Firstly, we measure the random lasing threshold and luminescence threshold of CsPbX_3 films pumped by an electron beam. Then, we simulate the spatial distribution of the electron beams in CsPbX_3 films. Combined with the above data, a low-frequency photon radiation conversion model based on the electron pumped perovskite quantum dots is presented. This could be a way to create a terahertz source with a high-power output or to multiply the terahertz power.

Keywords: electron beam, perovskite quantum dots, THz

PACS: 87.50.U–, 73.21.La **DOI:** 10.1088/1674-1056/ac8348

1. Introduction

Due to the limitations imposed by the gain bandwidth product (GBWP) of conventional solid materials and PN junction device structures, terahertz (THz) waves with sufficient power from emitting sources are essential for numerous applications in the fields of medicine, public safety, and communications technology.[1,2] One of the most prevalent continuous THz sources employing optical heterodyne generation (OHG) is a photomixer that can generate tunable and coherent THz signals at a low cost and low power consumption.[3,4] According to reports, the cutoff frequency of traditional photomixers has spanned multiple THz.[5,6] Only when a THz integrated antenna is in the diffusion region of a GaAs or InP PN junction, the minority of THz oscillation photocurrent generated by the PN junction[7,8] can be captured by an optical heterodyne down-conversion of two line-laser sources. Then, it will radiate forward space as a THz wave.[9,10] However, the construction of the device imposes intrinsic restrictions or limitations on the ability to increase the emitting power or efficiency. Typically, an increase in the size of the PN junction will directly increase the maximum yields of THz photocurrent. In the meantime, the increment will also nonlinearly increase the equivalent capacitance of the PN junction, and thus disrupt the impedance matching between itself and the integrated antenna. In the traditional semiconductor theory, it is hard to get around the limits between the bandwidth and output power of a terahertz source.

Academics have proposed numerous unique device designs and topologies for the construction of compact THz generating sources to alleviate the limits on high-power THz emission.[11–13] As a superior nonlinear absorber, CsPbX_3 is two orders of the magnitude larger than conventional quantum dots and has been utilized in a variety of light-emitting devices.[14–17] Thus, it has strong third-order nonlinear susceptibility and huge two-photon absorption cross-sections, which have been shown to produce THz radiation when ultrafast photons are used to generate random lasing.[18] According to Ref. [18], the polarized energy will be released in two forms following the movement of electrons from the valence band to the conduction band. As the dipole returns from the conduction band to the valence band for one form, the emitted energy consists primarily of visible photons or lasers. In addition, the low-frequency photon is emitted in the intraband of the conduction band via the "shift" dipole moment. In other words, this portion of the intraband energy will radiate as electromagnetic waves. In optically pumped experiments,

†Corresponding author. E-mail: muyining1985@hotmail.com
‡Corresponding author. E-mail: i.tafur.monroy@tue.nl
§Corresponding author. E-mail: fanhaibo1995@163.com
¶Corresponding author. E-mail: makram@nriag.sci.eg

© 2023 Chinese Physical Society and IOP Publishing Ltd

the conversion efficiency of a short-wavelength pulse laser to THz emission is significantly better than that of a near-infrared pulse laser. Interband transitions occur when numerous NIR photons simultaneously excite electrons in the valence band or when the pumping photon interval is shorter than the electron depolarization duration. The higher the excited electron energy relative to the valence band, the greater the efficiency of terahertz radiation. Consequently, the emission of photons with a low frequency should be the second-order effect of $CsPbBr_3$ random lasing. Improving the lasing efficiency and quality factor of $CsPbBr_3$ is crucial for low-frequency photon radiation power amplification. The primary methods for improving the random lasing efficiency and quality factor of $CsPbBr_3$ pumped by optics are to reduce the wavelength of the pumping laser,[19,20] shorten the pumping time gap,[21,22] and create complicated noncrystalline structures.[23–25] The most common way is by increasing the surface roughness of $CsPbBr_3$ films, which can affordably enhance the possibility of $CsPbBr_3$ nanocrystalline being simultaneously pumped by multiple photons.[26] To improve the lasing probability by raising the pump energy density of nanocrystals, whether it is to compress the pump time slot or to raise the surface roughness, which will surely increase the needless local thermal density and thermal effect interference. So, making each photon pump work better is a good way to improve how well low-frequency photon radiation works within the intraband.

Theoretically, the mobility of an electron in a vacuum is 100 to 1000 times greater than that of an electron in a solid, which satisfies the design requirements of a terahertz device. In addition, an electron with high kinetic energy in a vacuum can significantly enhance the efficiency of intraband low-frequency photon radiation for $CsPbBr_3$ compared to the UV pumping model. This study proposes utilizing the high energy electron beam (EB) in vacuum pump $CsPbBr_3$ films to improve the low-frequency photon radiation conversion efficiency, based on this hypothesis. A random lasing experiment proves the $CsPbBr_3$ perovskite quantum dot (PQD) films' random lasing features. Then, using the horizontal space optical function transfer experiment, we determine the luminescence threshold and luminescence area distribution of $CsPbBr_3$ films pumped by EB. Finally, simulation modeling and data fitting are used to figure out how well PQDs convert.

2. Materials and methods

2.1. PQDs preparation

According to the publication, $CsPbBr_3$ solutions were synthesized.[27] By using cesium oleate and lead bromide as precursors, $CsPbBr_3$ quantum dots were produced in an oil phase shielded by an inert gas via thermal injection and rapid ion exchange. After centrifugation and purification by high-speed centrifugation, $CsPbBr_3$ quantum dot solutions containing only inorganic metals were prepared with hexane as the solvent and a concentration of 10 mg/mL emitting green light. The conductive glass substrate was ultrasonically cleaned for 15 minutes with acetone, 100% ethanol, and deionized water, dried with a nitrogen gun, and placed in an 80 °C oven for 30 minutes. The prepared quantum dot solution was consistently stirred by a magnetic stirrer to produce a yellow-transparent $CsPbBr_3$ quantum dot spin-coating solution. We used a customized syringe to apply the quantum dot spin-coating solution to an indium tin oxide (ITO) conductive glass substrate, maintaining the homogenizing speed of 900 r/min for 5–10 s before dripping and 3500 r/min after dripping for 1020 s. Finally, spin coating produced a $CsPbBr_3$ PQD film that was uniformly transparent. By using a microelectronic analytical balance with a 0.01 mg resolution, the number of syringe droplets was calculated. The experiment demonstrates that, under specific conditions, the greater the spin-coating speed, the longer the gelling time, and the thinner the quantum dot layer.

The characteristic peaks shown in Fig. 1 are 15.1°, 21.5°, 30.4°, 34.2°, and 37.6°, respectively, corresponding to the crystal structures $\{0,0,1\}$, $\{1,1,0\}$, $\{0,0,2\}$, $\{2,1,0\}$, and $\{2,1,1\}$. That is consistent with the standard diffraction pattern obtained from the Joint Committee on Powder Diffraction Standards (JCPDS) database (No. 01-072-7929). That confirms the prepared QDs are $CsPbBr_3$. In addition, we characterized the $CsPbBr_3$ nanocrystals by transmission electron microscopy (TEM). The $CsPbBr_3$ nanocrystalline morphology effect used herein is shown in Fig. 2(a). Figure 2(b) shows the size distribution of the nanocrystals, which shows that the average size of the nanocrystals is about 15 nm. Scanning electron microscope images of $CsPbBr_3$ PQDs films with varying spin coating thicknesses are shown in Figs. 2(c)–2(g).

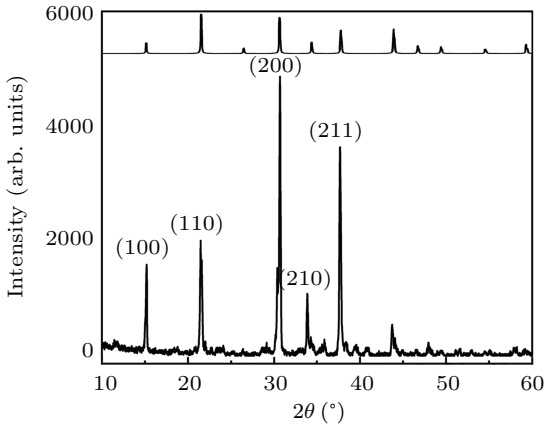


Fig. 1. XRD patterns of $CsPbBr_3$ nanocrystals.

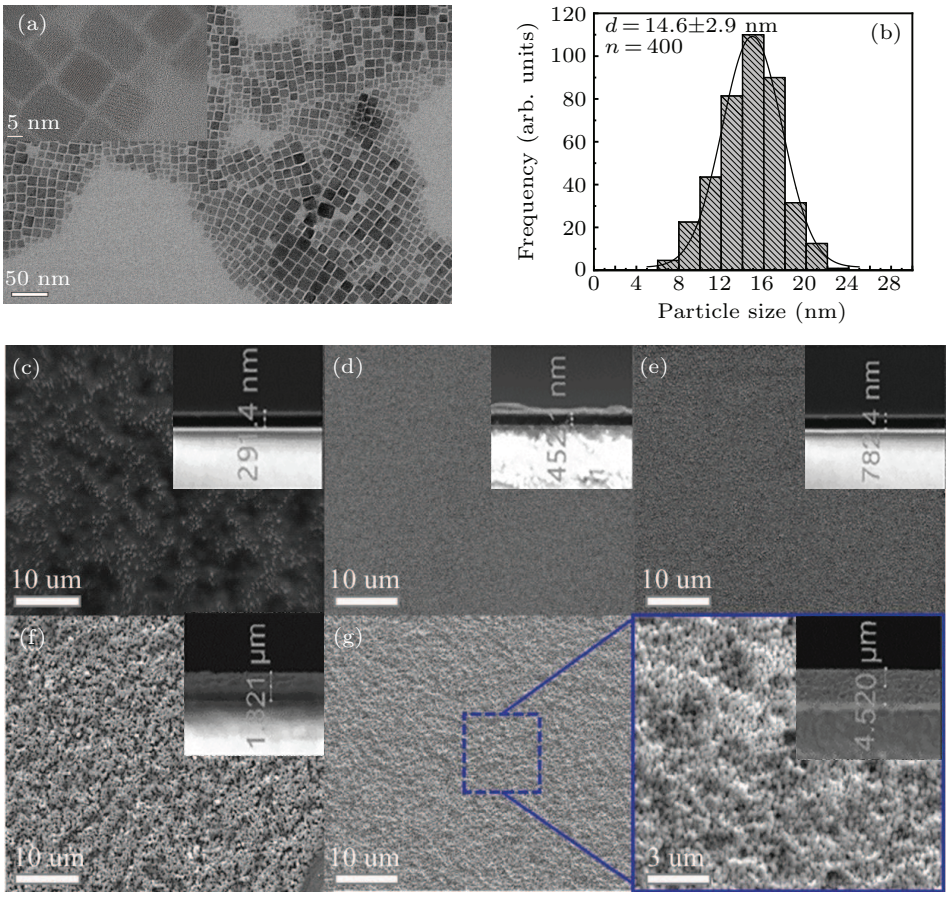


Fig. 2. (a) TEM characterization of $CsPbBr_3$ nanocrystals. (b) The size distribution of the nanocrystals. (c)–(g) SEM characterization of $CsPbBr_3$ perovskite thin films with thicknesses of 300 nm, 450 nm, 800 nm, 1800 nm, and 4500 nm.

2.2. Experimental methods

The sensitivity of the multi-alkali photocathode ($Na_2KSb(Cs)$) is slightly lower than that of the negative electron affinity photocathode (GaAs). But, the inclusion of additional metal elements in the photocathode film provides greater response time advantages. The photocathode's response time can approach sub-picosecond levels, satisfying the necessity for ultrafast EB generation.[28] In addition, the saturation current density output of the photocathode is extremely high in theory.[29] To avoid EB multi-path extension caused by high current density, the photocathode adopted for this work has a diameter of only 18 mm. The maximum output current intensity is less than 1 mA.

In the experiment of lasing characteristics, a 355 nm laser can be utilized as the trigger source. The PQD films and photocathode are positioned in a vacuum cavity with a vacuum level of 10^5 Pa. The UV laser triggers the photocathode from the top window of the vacuum cavity. The distance between PQD films and the photocathode is 20 cm to avoid vacuum breakdown. The PQD films are positioned on the detecting plane of the optical fiber connection system. The optical fiber coupling system connected spectrometer on integral to obtain random lasing spectrometer (Figs. 3(a) and 3(b)). Femtosecond spectrometer obtains PQDs luminescence transient properties (Fig. 3(c)). PIN detector obtains PQDs luminescence self-saturation properties (Fig. 3(d)).

In the experiment of optical transfer characteristics, the PQD films are positioned at the 40× magnification focal plane of the microscope. The microscope equipment is connected to a 5.6 m COMS camera. The sampling rate and precision of the CMOS sensor are around 140 nm, which is much superior to the 550 nm optical transferability of the microscope. On the surface of PQD films, a metal film net is put in, which can restrict pumping EB to shape spatial frequency information for PQDs luminescence. By watching how the loss of spatial frequency information changes, it is possible to show that EB horizontal scattering causes luminescence and indirectly estimates the luminescence threshold.

2.3. Casino stimulation

The PQD films were formed as 14 nm cubic nanocrystals, and each nanocrystal block simultaneously formed clusters of less than 300 nm. The incident direction of EB is vertical concerning the PQD films. The depth of secondary electron emission in common materials is less than 10 nm, which is significantly less than the thickness of PQD films. In this simulation, the energy loss of secondary electron emission is therefore disregarded. The electron's average kinetic energy distribution is calculated and represented by using the cylindrical coordinate

system (R, Φ, Z). The distribution of kinetic energy in PQD films is rotationally symmetric about the Z-axis, and the azimuth angle coordinates are compressed. The density of kinetic energy $\omega(R,Z)$ captured by each layer of PQD films can be formulated as follows:

$$\omega(R,Z) = \frac{E(R,Z)}{2\pi \cdot \Delta R \cdot R \cdot \Delta Z}, \tag{1}$$

where $E(R,Z)$ represents the kinetic energy captured at the horizontal diffusion distance R and vertical diffusion distance Z, and ΔR and ΔZ represent the horizontal and vertical sampling distances, respectively.

3. Results

3.1. Lasing characteristics

During the EB transition from vacuum to PQD films, backward or Rayleigh scattering predominates in the scatting process. The majority of EB and energy will concentrate mostly on the film's surface. Therefore, the EB-polarized zone of luminescence and lasing can be approximated as a cone. When there is insufficient pumping current density, there is little or no overlap of polarized regions pumped by various electrons in space. As a result, the pumping current density has a linear relationship with laser intensity. In contrast, by increasing the pumping current density, more polarized regions are pumped with multiple electrons. That will cause the lasing intensity increase to decelerate and the PQD films to reach lasing saturation. For this principle, 200 nm PQDs films were subjected to the self-saturation lasing studies. A PIN detector records the lasing intensity from the bottom of PQD films as the pumping field and current density are increased. The outcomes of the experiment are shown in Fig. 3(d). Self-saturation current densities of PQDs pumped at 3 K, 4 K, and 5 K are approximately 34.4 pA/μm^2, 26.3 pA/μm^2 and 17.6 pA/μm^2, correspondingly.

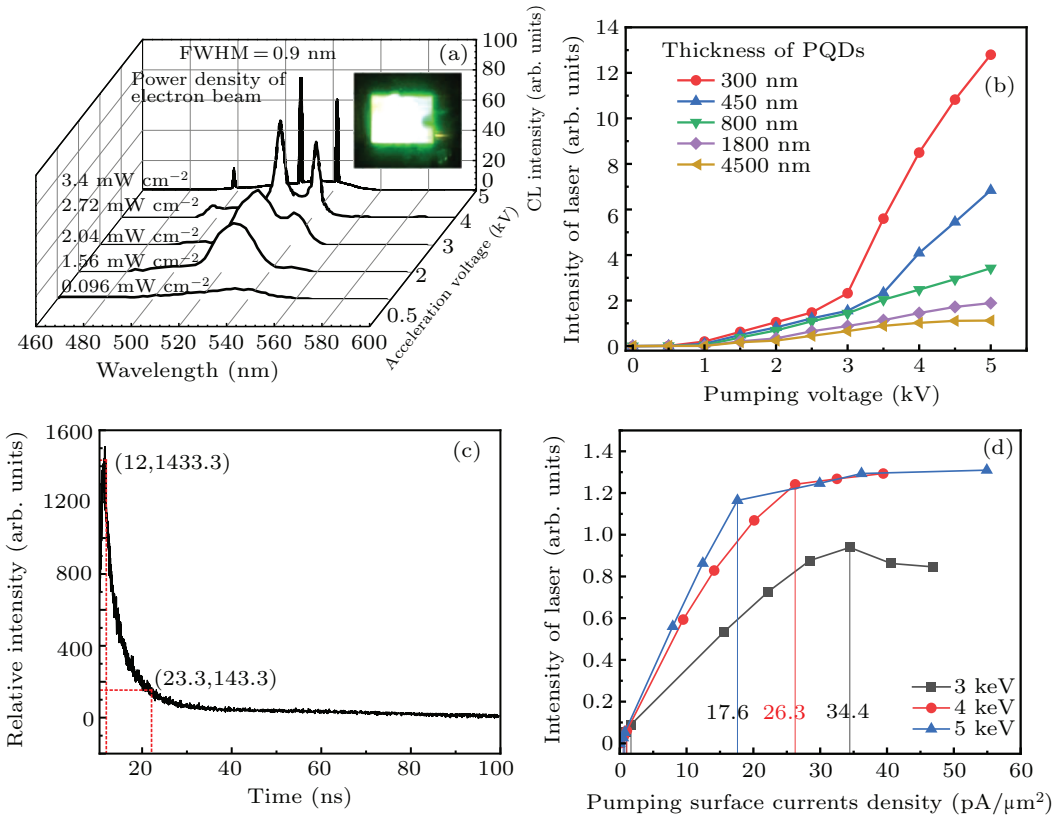


Fig. 3. (a) Spectrogram of PQDs pumped by EB with different EB surface densities, and the inset shows lasing of PQDs pumped by EB. (b) Lasing threshold of PQDs pumped by EB with changing pumping voltage. (c) Transient luminescence of the PQDs. (d) Self-saturation lasing experimental records of 200 nm PQDs films.

The data presented above illustrates three characteristics of the EB pumping model.[30,31] Firstly, a larger pumping field can directly increase the utilization rate of pumping current density based on the slope of Fig. 3(d) and decrease the pumping current density needed for self-saturation lasing in thin PQD films. Although the EB pumping source's bandwidth has reached the THz band,[32] electron focusing will still exhaust its bandwidth. The great utilization rate of pumping current density to trigger random lasing is extremely advantageous to the design of power-type EB devices at the THz level. It can effectively avoid excessive electron focusing. Secondly, the excessive pumping current density will increase the temperature of PQD films and lower the usage rate of pumping current density, as depicted in the saturation region of 3 keV data in Fig. 3(d). Compared to optical pumping, electron pumping may transport more energy into a larger region of PQDs, re-

sulting in a lower thermal density, which is advantageous when constructing a high-power device. However, once the PQD region was polarized to saturation, extra-pumping currents cause the luminescence efficiency to decrease because halide semiconductors are extremely temperature sensitive. Thirdly, the thickness of PQD films also affects their self-saturation lasing. For instance, since the sample film thickness is just 200 nm, the saturation lasing intensity of the 4 keV and 5 keV data coincided in advance.

To reduce the interplay among multiple pumping electrons in the PQDs films, we suppress EB pumping currents density at the nano Ampere per square millimeter to precisely control pumping laser intensity. As a result, there is no or very little time and space dependence of the PQDs polarization region caused by each pump electron in the experiments shown in Figs. 3(a)–3(c). The relationships between the lasing properties of the $CsPbBr_3$ films and pumping power density are shown in Fig. 3(a). Visibly, as the kinetic energy carried by the EB increases, the luminescence intensity of the $CsPbBr_3$ films is gradually enhanced. Furthermore, when the pumping voltage reaches 3 kV, some prominent random lasing peaks can be captured by the spectroscope. That is very similar to the random lasing effect of PQDs pumped by the laser pulse. Figure 3(b) shows the relationship between the lasing threshold or region and the EB pumping field. Namely, when pumping voltage reaches 3 kV, the lasing region will just touch a depth of 300 nm. Combined with the scattering distribution model, although tiny electrons can touch the depth of PQD films, most electrons and their energy can only stay at the surface layer of films. Moreover, most of the energy is concentrated in the region of several hundred nanometers. Namely, pumping electrons with high kinetic energy into the PQD films prefers horizontal scattering to vertical scattering. The luminescence intensity yielded by the tiny kinetic energy at the depth of films is so low that luminescence from the region is difficult to measure by the spectrograph. Therefore, we neglected the pumping kinetic energy located at the depth of PQD films. In addition, the transient luminescence property of the $CsPbBr_3$ films is also measured and shown in Fig. 3(c). The luminescence lifetime of its decay to $1/e$ is about 11.3 ns. There is no denying that the testing result in Fig. 3(c) is consistent with some academic reports.[33]

3.2. Optical transfer characteristics

Compared to the measurement of the lasing threshold, EB will horizontally scatter strongly and randomly in PQD films. That significantly complicates the direct and accurate measurement of its luminescence threshold. Consequently, based on the Abbe imaging principle, we take the advantage of the optical transfer characteristics of EB-pumped PQDs to indirectly estimate their luminescence region and threshold. Figure 4(a) depicts the characterization of the metal film-net by using the methods described previously.

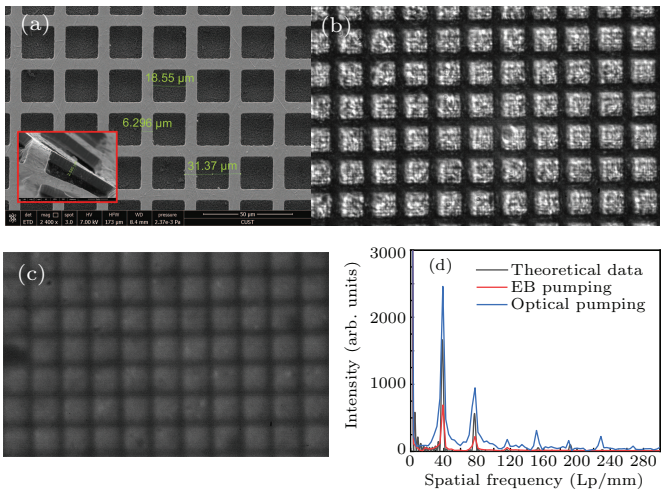


Fig. 4. (a) Space size of the metal film-net. (b) Luminescence imaging of PQDs pumped by laser. (c) Luminescence imaging of 300 nm PQD film pumped by 5 keV EB. (d) Spatial frequency spectrum comparison of both luminescence models.

At this point, the edge of luminescence under the metal film net will produce diffraction. After the luminescence of PQDs is imaged by the microscope, its two-dimensional porous diffraction information will be collected by CMOS. At the image side of the microscope, the metal film net and PQD films pumped by EB will produce typical Fraunhofer diffraction. The final imaging effects of PQDs luminescence pumped by a UV laser and EB with 5 keV kinetic energy are shown in Figs. 4(b) and 4(c). The space optical transfer effect of optical pumping is much superior to that of EB pumping. That convincingly demonstrates that the microscope system's optical resolution can satisfy the requirements of measuring EB scattering distribution in the PQD films. Furthermore, as shown in Fig. 4(a), the spatial frequency function of the metal film-net is a typical two-dimensional grating. Its theoretical system function can be written as

$$I(x,y) = I(0,0)\,\mathrm{SinC}^2\left(\frac{ax}{\lambda f}\right)\left[\frac{\sin N\left(\frac{\pi xd}{\lambda f}\right)}{\sin\left(\frac{\pi xd}{\lambda f}\right)}\right]^2 \times \mathrm{SinC}^2\left(\frac{ay}{\lambda f}\right)\left[\frac{\sin N\left(\frac{\pi yd}{\lambda f}\right)}{\sin\left(\frac{\pi yd}{\lambda f}\right)}\right]^2, \quad (2)$$

where $\mathrm{SinC}(u) = \sin(\pi u)/\pi u$, $I(0,0)$ is the central main maximum intensity, a is the length of the gate hole, λ is the wavelength, f is the focal length of the lens, N is the number of gate holes, and d is the gap of the gate hole.

Consequently, the spatial frequency spectrum of the EB luminescence model can be measured and is illustrated in

Fig. 4(d). To simplify the analysis, only the one-dimensional nature of the frequency function is examined. In addition, based on the spatial frequency properties of the metal film net, its fourth and eighth-order spatial frequency spectrum should vanish. Thankfully, the fourth-order and eighth-order spatial frequency spectrum have not completely vanished because of minuscule manufacturing flaws in the metal film net. The comparative effects of the frequency spectrum, including both the luminescence model and the theoretical model, are depicted in Fig. 5. Visibly, the characteristic frequency of imaging pumped by EB reaches only the fourth-order, which is less than half of that pumped optically. This conclusion is also supported by a comparison of the edge gradients of both luminescence models. As shown in Fig. 5, the resolution of the CMOS pixel and optical diffraction of the microscope cause the metal film-net bridge to extend horizontally by approximately 820 nm. EB scattering in the horizontal direction ought to result in an additional 850 nm extension of the edge gradient compared with optically pumped imaging. Therefore, the horizontal scattering depth of EB is approximately 850 nm. Specifically, the average kinetic energy density absorbed by PQDs at this horizontal depth (850 nm) should be the luminescence threshold. In this area, the $CsPsBr_3$ nanocrystals can take in enough EB energy to send out a visible photon.

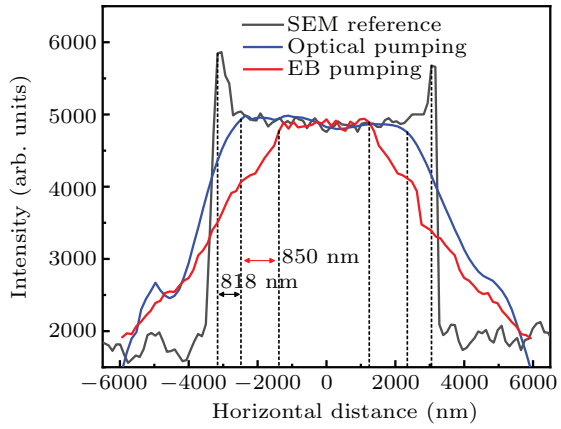


Fig. 5. Edge gradient comparison of both luminescence models.

4. Discussion

In the preceding experiments, the lasing threshold, luminescence threshold, and polarized spatial distribution have been approximated modeling the conversion efficiency of low-frequency photons in the various PQD film layers. We utilized Casino software to simulate the multiple scattering of EB in the different layers of a film.[34] Simulating the lasing regions of PQD films is possible by assuming different lasing thresholds. By comparing the distribution feature of the lasing region with experimental data, it is possible to precisely fit the energy distribution of the lasing region in actual films.

Figure 6(a) shows how much vertical kinetic energy each layer of PQD films can capture. In addition, Fig. 6(b) illustrates the horizontal kinetic energy density captured by each PQD film layers. Secondly, lasing and luminescence experimental results in both directions can confirm threshold limits. In Fig. 6(c), a cylindrical coordinate model of polarized distribution in PQD films pumped by 5 keV can be constructed based on both boundaries. When the volume density of pumping energy in the film layers reaches about 20 eV/μm^3, the PQDs region will enter luminescence. For the PQD film layers to enter the lasing mode, the volume energy density must reach about 237 eV/μm^3. The volume variation of the PQD lasing region under different pumping kinetic energies and current densities corresponds to the lasing intensity curves of Figs. 3(c) and 3(d), respectively. In other words, all experimental results and simulation data are comparable, with comparison effects depicted in Figs. 6(d) and 6(e).

Microscopically, the bulk material of PQDs has a typical centrosymmetric structure. Despite this, numerous crucial factors will disrupt the inversion symmetry.[35] Pb lone pair, sample defects, and surface effects are examples. Experiments typically reveal the Rashba effect or second harmonic generation.[36,37] $CsPbBr_3$ has a typical direct bandgap structure, which is well known. The ultrafast excitation source pumps $CsPbBr_3$ into the conduction band. In $CsPbBr_3$, the Br p-orbital contributes most to the valence band, whereas the Pb p-orbital contributes most to the conduction band. When $CsPbBr_3$ enters the conduction band, the electron densities on both sides of Pb are inconsistent, causing the lattice charge center to shift in tandem with the Pb mass center shift. The asymmetry of the electron density surrounding the Pb atom indicates that the cation displacement will disrupt the local symmetry in $CsPbBr_3$ and produce a high-order shift currently.[38] Figures 7(a) and 7(b) depict the depolarization of $CsPbBr_3$. Once a high-energy electron polarizes a $CsPbBr_3$ lattice, a (virtual) electron and a (virtual) hole are located in the conduction band and valence band, respectively. As shown in Fig. 7(a), the low-frequency photon radiation is generated by the "shift" dipole moment. As shown in Fig. 7(b), as the electron and hole recombine, a visible photon is emitted and energy is once again conserved. Once an electron with high kinetic energy enters $CsPbBr_3$ films, its conversion efficiency of low-frequency photon radiation is directly related to its macro location within the films. With increasing electron incidence depth, the electron's kinetic energy will decrease, resulting in a decline in energy conversion efficiency. To figure out how well low-frequency photon radiation can be turned into other types of radiation, the kinetic energy decay of electrons in $CsPbBr_3$ films needs to be studied quantitatively.

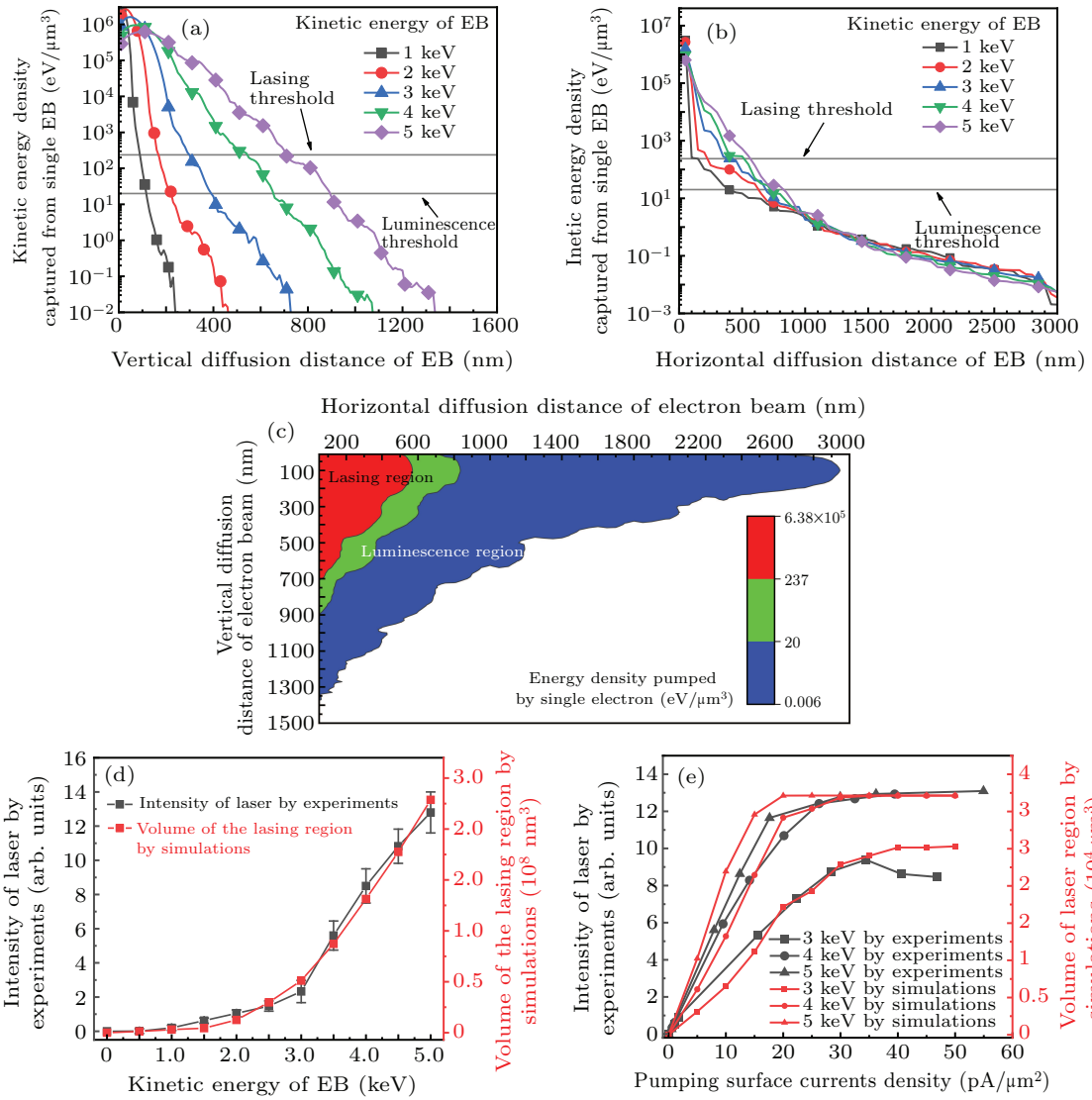


Fig. 6. The energy distribution is captured from EB in the different layers of PQDs films in the vertical direction (a) and horizontal direction (b). (c) Polarized distribution model in the PQDs films pumped by 5 keV. (d) The intensity laser of 300 nm PQDs contrast between simulated results and experimental data. (e) Self-saturation lasing of 200 nm PQDs contrast between simulated results and experimental data.

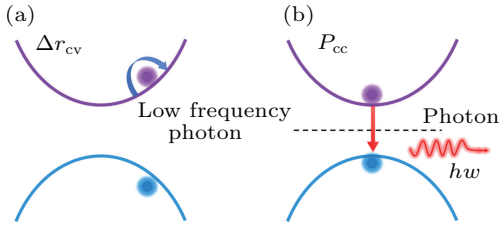


Fig. 7. (a) Low-frequency photon radiation model. (b) Visible photon radiation model.

The low-frequency photon radiation is a secondary-order effect of random lasing, as demonstrated by the preceding theoretical analysis. Only if there is random lasing will the low-frequency photon be produced. The energy of each photon emitted by an interband transition during random lasing or luminescence is nearly identical. On this basis, the theoretical conversion efficiency of low-frequency photon radiation in the lasing region is immediately calculable by inserting the lasing threshold into the above polarized PQDs spatial distribution with a 5 kV pumping voltage, as depicted in Fig. 6(c).

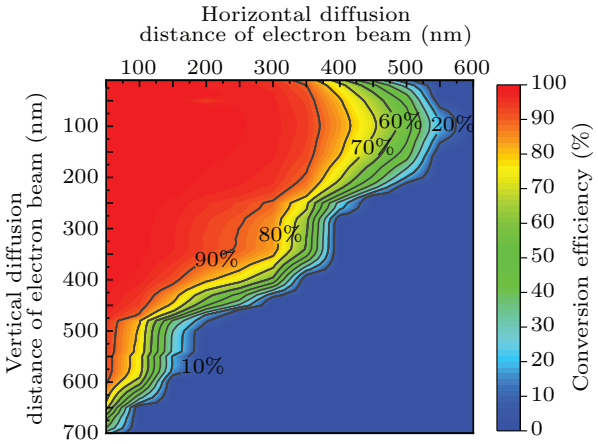


Fig. 8. Conversion efficiency distribution of low-frequency radiation.

Theoretically, due to the thermal effect of the small injection current model, the highest conversion efficiency in the random lasing region can exceed 99% close to the incident interface. However, as the EB incident depth increases, the con-

version efficiency will decrease until it reaches the boundary of the lasing region. In addition, the energy of regions other than the lasing region does not contribute to the energy of low-frequency photon radiation. Therefore, the higher pumping field can polarize the larger PQDs lasing region and achieve a higher conversion output power for low-frequency photon radiation in terms of whole film layers. Based on the polarized PQDs spatial distribution model of Fig. 6, Fig. 8 depicts the final 2D conversion efficiency model of 5 keV low-frequency photon radiation.

5. Conclusions

This paper argued both these strengths for taking advantage of PQDs pumped by EB to generate low-frequency photon radiation. Firstly, EB with high kinetic energy can amplify the secondary-order effect of random lasing in the PQD films, making power multiplication possible for THz low-frequency photon emitting. Secondly, when compared to the optically pumped model, the kinetic energy of EB pumping can penetrate the innermost PQD films. Vacuum electrons can polarize large regions in the PQD films, greatly reducing the thermal density of the pumping process throughout the films. That is advantageous to the manufacturing and design of power-type devices. So, the low-frequency photon radiation that this paper looks at could be a way to make THz high-power emitting sources or to multiply terahertz power.

Acknowledgements

This work is funded by the National Natural Science Foundation of China (Grant Nos. 61905026, 61703057, 11874091, and 61905023), the National Key Research and Development Program of China (Grant No. 2018YFB1800303), Construction Project of Key Laboratory of Astronomical Optics Technology of Chinese Academy of Sciences (Grant No. CAS-KLAOTKF201803), Chongqing Natural Science Foundation of China (Grant No. CSTC2021JCYJ-MSXMX0500), and Foundation Project of Jilin Province, China (Grant Nos. 20210402067GH, JJKH20210830KJ, JJKH20210800KJ, 20200301065RQ, 20190201188JC, and 2019C043-6).

References

[1] Minamide H 2015 *IEEE T. THz Sci. Techn.* **5** 1104
[2] Lee A J, Spence D J and Pask H M 2020 *Prog. Quant. Electronics* **7** 100254
[3] Hubers H W, Richter H, Eichholz R, Wienold M, Biermann K and Schrottke L 2017 *IEEE J. Sel. Top Quant.* **23** 1
[4] Chen S Q, Xie Z Q, Liu J M, He Y L, Cai Y, Zhang X K, Xiao J N, Li Y and Fan D Y 2017 *Adv. Cond. Matter Phys.* **7** 1
[5] Yang S H, Watts R, Li X, Wang N, Cojocaru V and Gorman J O 2015 *Opt. Express* **23** 31206
[6] Ironside D J, Salas R, Chen P Y, Le K Q and Bank S R 2019 *Opt. Express* **27** 9481
[7] Raab J, Mezzapesa F P, Viti L, Dessmann N and Vitiello M S 2020 *Nat. Commun.* **11** 4290
[8] Dai J, Ruan C J, Ding Y and Yan Z 2020 *Opt. Express* **29** 409879
[9] Alibakhshikenari M, Virdee B S, Khalily M, Chan H S and Limiti E 2020 *IEEE Antenn. Wirel. Pr.* **19** 1576
[10] Dukhopelnykov S V, Lucido M, Sauleau R and Nosich A L 2021 *IEEE J. Sel. Top Quant.* **27** 1
[11] Belkin M A and Capasso F 2015 *Phys. Scr.* **90** 118002
[12] Yardimci N T, Cakmakyapan S, Hemmati S and Jarrahi M 2017 *Sci. Rep-Uk.* **7** 4166
[13] Fujita K, Hayashi S, Ito A, Hitaka M and Dougakiuchi T 2019 *Nanophotonics* **8** 2235
[14] Lin S S, Lin H, Chen G X, Wang B, Yue X M, Huang Q G, Xu J, Cheng Y and Wang Y S 2021 *Laser Photonics Rev.* **15** 2100044
[15] Yan D D, Shi T C, Zang Z G, Zhao S Y, Du J and Leng Y X 2020 *Chem. Eng. J.* **401** 126066
[16] Mo Q H, Chen C, Cai W S, Zhao S Y, Yan D D and Zang Z G 2021 *Laser Photonics Rev.* **15** 2100278
[17] Lan S G, Peng Y Y, Shen H Z, Wang S, Ren J W, Zheng Z P, Liu W W and Li D H 2021 *Laser Photonics Rev.* **15** 2000428
[18] Hang H Y, Su R, Huang Y Y, Zhou Y X, Zhao Q Y, Khurgin J B, Xiong Q H and Xu X L 2019 *Adv. Funct. Mater.* **29** 1904694
[19] Wang Y, Li X, Zhao X, Xiao L, Zeng H and Sun H 2015 *Nano Lett.* **16** 448
[20] Fu Y, Zhu H, Stoumpos C C, Ding Q, Wang J and Kanatzidis M G 2016 *ACS Nano* **10** 7963
[21] Ren Y, Wang W, Wang Z, Xia S and Wang Y 2020 *J. Phys. Chem. C* **124** 8341
[22] Park Y, Ying G, Jana A, Osokin V and Kim K S 2014 *Nano Res.* **14** 108
[23] Mu Y, Zhang T, Chen T, Tang F and Li P 2019 *Nano* **15** 2050016
[24] Hu Z, Li C, Tang X, Leng Y, Sun K and Zang Z 2017 *Nano Energy* **40** 195
[25] Qaid S M H, Alharbi F H, Bedja I, Nazeeruddin M K and Aldwayyan A S. 2020 *Nanomaterials* **10** 1605
[26] Wu Z, Chen J, Mi Y, Sui X, Zhang S, Du W, Wang R, Shi J, Wu X, Qiu X, Qin Z, Zhang Q and Liu X 2018 *Adv. Opt. Mater.* **6** 1800674
[27] Kim J, Manh N T, Thai H T, Jeong S K, Lee Y W, Cho Y, Ahn W, Choi Y and Cho N 2022 *Nanomaterials* **12** 920
[28] Dong T W and Xun H 2012 *Acta Phys. Sin.* **61** 187901 (in Chinese)
[29] Romanov R, Fominski V, Demin M, Fominski D, Rubinkovskaya O, Novikov S, Volkov V and Doroshina N 2021 *Nanomaterials* **11** 1461
[30] Ren H, Mu Y N, Du P, Li Y Z, Fan H B, Wang S, Idelfonso T M, Ibrahim M 2022 *Acta Opt. Sin.* **42** 1927001
[31] Fan H B, Mu Y N, Liu C Y, Zhu Y, Liu G Z, Wang S, Li Y Z and Du P 2020 *Chin. Opt. Lett.* **18** 011403
[32] Dolgov A K, Ushakov D V, Afonenko A A, Dyuzhikov I N, Glinskiy I A and Ponomarev D S 2021 *Quantum Electronic* **51** 164
[33] Bao Z, Wang W, Tsai H Y, Wang H C, Chen S and Liu R S 2020 *J. Mater. Chem. C* **8** 1065
[34] Demers H, Poirier-Demers N, Jonge N D and Drouin D 2011 *Scanning* **17** 612
[35] Hussain M, Rashid M, Saeed F and Bhatti A S 2021 *J. Mater. Sci.* **56** 528
[36] Korolev V I, Pushkarev A P, Obraztsov P A, Tsypkin A N and Makarov S V 2019 *Nanophotonics* **9** 187
[37] Chen J, Wu K, Hu W and Yang J 2021 *J. Phys. Chem. Lett.* **12** 1932
[38] Cinquanta E, Meggiolaro D, Motti S G, Gandini M, Alcocer M and Akkerman Q A 2019 *Phys. Rev. Lett.* **122** 166601